JMEPEG (2020) 29:7899–7907
https://doi.org/10.1007/s11665-020-05313-8

1059-9495/$19.00

Pressureless Sintering Kinetics of $NiFe_2O_4$ Ceramic Fabricated by Slip Casting

Zhigang Zhang, Zhuokun Cao, Guoyin Zu, and Jianrong Xu

Submitted: 30 June 2020 / Revised: 21 October 2020 / Accepted: 1 November 2020 / Published online: 16 November 2020

In this work, a systematic research is carried out to investigate the sintering kinetics of $NiFe_2O_4$ ceramic obtained by slip casting and pressureless sintering. The sintering shrinkage behaviors showed the linear shrinkage and linear shrinkage rate of the green body in the axial and radial directions, both increased with increasing sintering temperature, though the maximum linear shrinkage rate in the radial direction was acquired at a lower temperature (1280.7°C) than that in the axial direction (1305.4°C) for a denser compact. The temperature related to the maximum densification rate was about 1316.5°C while the relative density was around 72%. The characteristic sintering kinetics window exhibited that the sintering process could be typically divided into three stages. The sintering activation energy of the initial stage was 268.34 kJ mol^{-1}, and the initial stage of the sintering process was controlled by both grain boundary diffusion and volume diffusion mechanisms. The grain growth kinetic analysis illustrated the grain growth exponent (n) reduced from 2.959 to 2.169 when the sintering temperature increased from 1300 to 1375°C, while the activation energy for grain growth decreased with both the increasing of sintering temperature and the shortening of holding time. It implied that the atomic diffusion process controlled the grain growth. In addition, it was observed that increases in the bending strength and elastic modulus reached its maximum value of 70.36 ± 1.03 MPa and 3.44 ± 0.53 GPa, respectively, mainly associated with the relatively dense microstructure.

Keywords activation energy, densification, grain growth, kinetics, nickel ferrite

1. Introduction

$NiFe_2O_4$ is a typical mixed valence metal oxide with an inverse spinel structure, where the tetrahedral sites are occupied by Fe^{3+} cations, and the octahedral sites are equivalently occupied by Fe^{3+} and Ni^{2+} cations (Ref 1-3). Due to the superior and unique structure of this material, $NiFe_2O_4$ has been widely applied in magnetic materials (Ref 4, 5), catalyst (Ref 6, 7), high sensitive gas sensors (Ref 8, 9), microwave devices (Ref 10), supercapacitors (Ref 11, 12) and high temperature electrode material (Ref 13, 14). Production of nickel ferrite bulk ceramics with high performances gained increasing interests on account of the prospective applications.

It has been well-known that the microstructure (mainly density and grain size) is an essential ingredient of ceramic materials, therefore the microstructure plays a precedence role in the properties of $NiFe_2O_4$ ceramics (Ref 15). In the process of preparing ceramics by powder metallurgy, sintering is the crucial stage that determines the final microstructure of the dense $NiFe_2O_4$ ceramics because it masters the process of morphological evolution at high temperature. Traditionally, densification and grain growth are two competing processes in sintering (Ref 16). The properties of polycrystalline materials would be improved by higher density meanwhile being degraded by the undesirable grain growth. It is uneasy to control the sintering kinetics window for $NiFe_2O_4$ ceramics because of the extreme difficulty in fulfilling complete densification and restricting grain growth at the same time.

By reason of the low sintering rate of spinel (Ref 17), it is a difficult task to eliminate the pores of ceramic materials, especially for removing large pores derived from the forming process. The sintering densification behavior is highly sensitive to microstructure of the green compact, such as particle size, pore size, agglomeration and homogeneity. The density and microstructural homogeneity of the sintered ceramics can be notably improved by homogeneity of green compact with high density. Slip casting is colloidal and cost-effective method of fabricating the homogeneous and defect-free green compact for sintering process (Ref 18-21). Previous research showed that higher density $NiFe_2O_4$ ceramics with better homogeneity can be prepared by using slip casting when compared to cold pressing (Ref 22). Also, the temperature associated to maximum linear shrinkage rate and the sintering activation energy of the initial sintering stage of slip casted green body were both lower than these of cold pressed compact, owing to high density and homogeneity of the slip casted green body. However, up to now, the detailed information about the sintering densification and grain growth behaviors of $NiFe_2O_4$ ceramics obtained by slip casting and pressureless sintering has not yet been reported. The intensive understanding of the sintering mechanism is of vital importance for controlling the densification process of the $NiFe_2O_4$ ceramics, and grain growth kinetics, which was used to control the microstructural features, e.g., shape, size and distribution of grains, could be

Zhigang Zhang, Zhuokun Cao, and **Jianrong Xu**, School of Metallurgy, Northeastern University, Shenyang, China; and Key Laboratory for Ecological Metallurgy of Multimetallic Mineral (Ministry of Education), Northeastern University, Shenyang, China; and **Guoyin Zu**, School of Materials Science and Engineering, Northeastern University, Shenyang, China. Contact e-mail: zhangzg@smm.neu.edu.cn.

optimized through deep insight into the grain growth rate and growth mechanism. It is therefore essential to adjust the final microstructure of the $NiFe_2O_4$ ceramics for the desired performance through detailed understanding sintering kinetics of $NiFe_2O_4$ ceramics.

The present investigation aimed to study sintering behaviors of $NiFe_2O_4$ ceramic obtained by slip casting and pressureless sintering. The characteristics of microstructure evolution and the phenomenological analysis of grain growth kinetics during sintering were emphatically studied to understand intensively the sintering mechanism and optimize microstructural features. Besides, mechanical properties of $NiFe_2O_4$ ceramics were also partially investigated.

2. Experimental

2.1 Materials

Analytical reagents, namely ferrous sulfate heptahydrate ($FeSO_4{\cdot}7H_2O$, ≥ 99.0%), nickel sulfate hexahydrate ($NiSO_4{\cdot}6H_2O$, ≥ 98.5%), sodium chloride (NaCl, ≥ 99.5%), sodium hydroxide (NaOH, ≥ 96.0%), nickel monoxide (NiO, ≥ 99.0%) and iron oxide (Fe_2O_3, ≥ 99.0%), were bought from Sinopharm Chemical Reagent Co., Ltd., Shanghai, China. An analytical nano-binder was purchased from Jiangsu Jiuchuan Nanomaterials Technology Co., Ltd., Huaian, China. The nano-binder, consisting mainly of SiO_2, $Al_2Si_4O_{10}$, Al_2O_3 and $MgO{\cdot}Al_2O_3{\cdot}SiO_2$, can also be defined as attapulgite clay nanopowder.

Planetary ball-milling assisted solid-state reaction process was employed to prepare $NiFe_2O_4$ nanoparticles (Ref 23). Firstly, stoichiometric molar amounts of $FeSO_4{\cdot}7H_2O$, $NiSO_4{\cdot}6H_2O$ and NaOH with 20 wt.% NaCl as dispersant were planetary ball-milled at room temperature to prepare precursors. Then, the precursors were calcined at 750°C for 1 h and washed away the inorganic salts to obtain pure $NiFe_2O_4$ nanoparticles.

$NiFe_2O_4$ powders were synthesized by high-temperature solid-state reaction. The well-mixed stoichiometric NiO and Fe_2O_3 powders were cold pressed under 60 MPa and then air-calcined at 1200°C for 6 h to form $NiFe_2O_4$ bulk materials. The sintered bulk matrix materials were crushed and screened to obtain $NiFe_2O_4$ powders with particle sizes below 74 μm.

The mixtures of 82.5 wt.% $NiFe_2O_4$ powders, 12.5 wt.% $NiFe_2O_4$ nanoparticles and 5 wt.% nano-binder were mixed on a planetary miller (KWQ-X4B/B, Jinhong, China) with deionized water as a solvent. The mixtures were ball-milled with a revolution speed of 48 r/min and autorotation rate of 72 r/min for 24 h to prepare the slurries with a solid content of 56 wt.%. Characteristics of the raw materials of slurry, namely $NiFe_2O_4$ powder, $NiFe_2O_4$ nanoparticle and nano-binder, are listed in Table 1.

The as-prepared slurry was directly slip casted into plaster molds for the production of Φ10 × 15 mm cylinders at room temperature. The cast solids were taken away from the mold and naturally dried. The dried green bodies were finally calcined in a self-made high-temperature sintering furnace with the maximum sintering temperature of 1600°C under air atmosphere. The calcination parameters, such as temperature, heating rate and dwell time, would be presented in subsequent studies.

2.2 Characterization

The densification behaviors of the green compacts were measured with a horizontal dilatometer (DIL 402 PC, Netzsch, Germany). The relative density of sintered samples was measured according to the Archimedes principle using distilled water as medium. The bending strength was determined by a three-point method using an electronic universal testing machine (4206-006, Instron, USA) at ambient temperature with a compression speed of 0.5 mm/min. The microstructure of the sintered samples was examined by means of field emission scanning electron microscopy (FESEM; Ultra Plus, Zeiss, Germany). The SEM micrographs of the polished and etched samples were elaborated by the Image-Pro Plus software and more than 300 grains were selected to determine grain sizes.

3. Results and Discussion

3.1 Sintering Densification Behavior

The linear shrinkage during sintering can reflect the sintering densification process and the variation tendency of relative density of sintered materials to some extent. Figure 1 shows the linear shrinkage ($\Delta L/L_0$) and linear shrinkage rate ($d(\Delta L/L_0)/dt$) of the $NiFe_2O_4$ ceramic green body from ambient temperature to 1500°C during sintering at a constant heating rate of 5°C/min. The linear shrinkage and linear shrinkage rate of the green bodies in the axial and radial directions exhibited very similar trends, although the maximums were somewhat different. The maximum linear shrinkage of the green body in the radial direction was a bit lower than that in the axial direction, whereas the maximum linear shrinkage rate in the radial direction was slightly higher than that in the axial direction. Moreover, the temperature related to the maximum linear shrinkage rate in the radial direction was 1280.7°C, which was lower than that in the axial direction (1305.4°C). The green body was denser along the radial direction than along the axial direction, owing to the obvious hygroscopicity

Table 1 Characteristics of the raw materials of slurry

Materials	Particle size (D_{50}), μm	Morphology
$NiFe_2O_4$ powder	28.574 ± 1.662	Multishaped
$NiFe_2O_4$ nanoparticle	0.061 ± 0.019	Spherical and polyhedral
Nano-binder	0.074 ± 0.023	Needle whisker
Slurry	9.300 ± 0.840	…

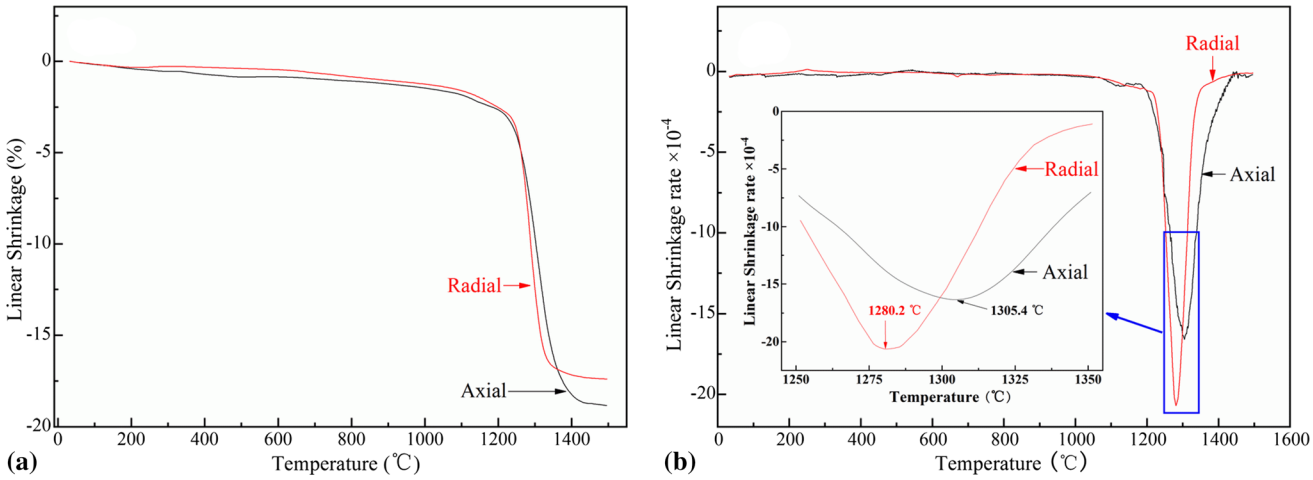

Fig. 1 Linear shrinkage (a) and linear shrinkage rate (b) of the $NiFe_2O_4$ ceramic green body in the axial and radial directions sintered at a heating rate of 5°C/min

of porous plaster mold. The linear shrinkages were less than 2.5% in both directions when the temperature was lower than 1100°C, implying inconspicuous densification. When the preform sintering temperature was increased from 1100 to 1400°C, the linear shrinkages in both directions increased gradually. There was little effect of sintering temperature on the densification when the temperature was over 1400°C for the insignificant further linear shrinkage. The linear shrinkage rates, exhibited broad peaks for both the axial and radial directions between 1200 and 1400°C, with maximum at approximately 1300°C.

The relative density of the sintered specimen can be calculated from the linear shrinkage during sintering as follow (Ref 24):

$$\rho = \frac{\rho_1}{\rho_0\left[1-(\Delta L/L_0)_R\right]\left[1-(\Delta L/L_0)_A\right]^2} \quad \text{(Eq 1)}$$

where ρ is the relative density of the sintered specimen; ρ_1 is the bulk density of the green body (calculated by measuring the volume and mass of the green body, 2.59 g cm^{-3}); ρ_0 is the theoretical density of the green body (estimated using the rule of mixture, 5.21 g cm^{-3}), and $(\Delta L/L_0)_R$ and $(\Delta L/L_0)_A$ are the linear shrinkage of the green body in the radial and axial directions, respectively. The sintering temperatures were selected between 1150 to 1450°C because sintering shrinkage was negligible below 1150°C and above 1450°C.

Figure 2 shows the relative density and densification rate in the sintering temperatures of 1150-1450°C. The instantaneous relative density was calculated using formula (1). To determine the effect of sintering temperature on the microstructure evolution, the $NiFe_2O_4$ ceramic green bodies were sintered at 5°C/min from room temperature to 1250, 1300, 1350, 1400 and 1450°C, respectively, with 3 min holding at the peak temperature. The fracture morphologies of the samples were characterized by FESEM, and the relative densities were tested using the Archimedes method. The relative density averages of five samples were shown in Fig. 2(a) by red solid squares. The obtained relative density values differed slightly from those obtained using formula (1); the maximum difference was only 2.19% at 1400°C, indicating that the accuracy and reliability of these two methods of calculating the relative density were acceptable. The densification was relatively low at the temperatures below 1250°C for the small increase of relative density. At the temperature of 1250°C, as shown in the insets of Fig. 2(a), a mass of open pores existed in the ceramic material, and the grains mainly retained their original morphology. As the sintering temperature increased, the SEM images revealed the growth of a sintering neck, in which the interparticle distance became shorter, and the grain boundary bonding strength became higher. As a result, the grain size increased, and the porosity decreased. The maximum relative density was obtained at 1400°C, and then the density improvement can be negligible with further increase in temperature. When the temperature was above 1400°C, the grain growth predominated in the competition of densification and grain growth. When the temperature was 1450°C, the interfacial bonding strength was so considerably high that transgranular fracture occurred. However, the relative density of the sample sintered at 1450°C, obtained from Archimedes method, was slightly lower than that of the sample sintered at 1400°C, on account of the formation of intracrystalline pores at higher temperature. The sintering densification rate was enhanced for the higher sintering activity at elevated temperature. Some pores were not filled completely during grain boundary migration and partially existed in newly generated grains. So the intracrystalline pores were formed.

As presented in Fig. 2(b), densification rate ($d\rho/dT$) first increased and then decreased with increasing temperature, and the maximum densification rate was obtained at about 1316.5°C, which was both higher than that of the maximum linear shrinkage rate in the radial and axial directions. The densification rate ($d\rho/dt$) versus relative density was exhibited in Fig. 2(c). When the relative density was around 72%, the highest densification rate ($d\rho/dt$) was achieved.

The pressureless sintering kinetics window was shown in Fig. 3. According to the literatures (Ref 25, 26), the sintering process could be principally divided into three stages: (I) the initial stage (relative density $<$ 59.14%, $<$ 1275°C): the relative linear shrinkage was not more than 5%, and the grain growth did not obviously occur. Particle rearrangement controlled this stage, and the density increased mainly for the close packing of the particles, including grain sliding and rotation. (II): the intermediate stage (relative density between 59.14 and 88.78%, 1275-1375°C): the grains were beginning to grow and

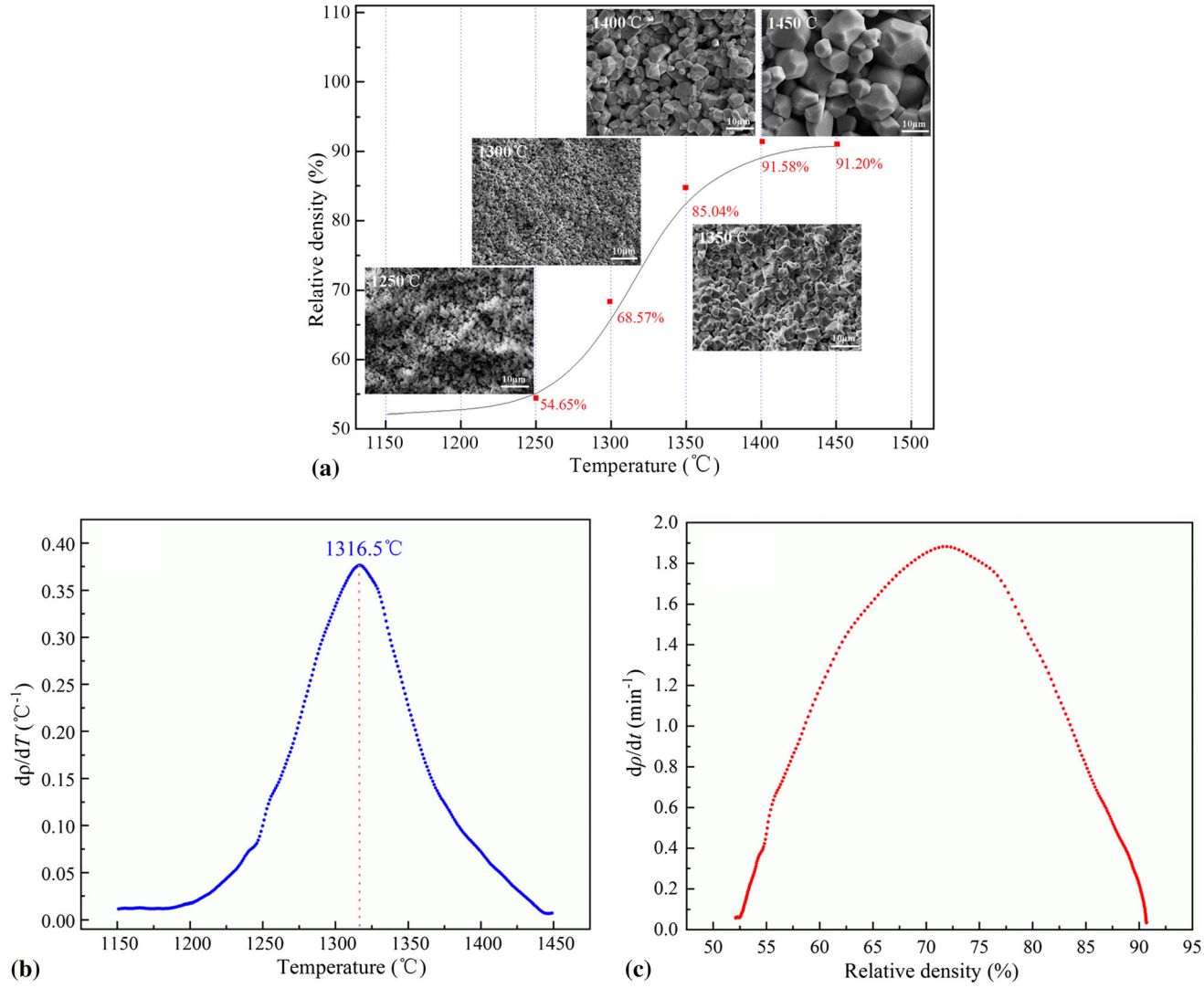

Fig. 2 Temperature dependence of relative density (a) and densification rate (dρ/dT) (b), densification rate (dρ/dt) as a function of relative density (c) of $NiFe_2O_4$ green compacts during sintering

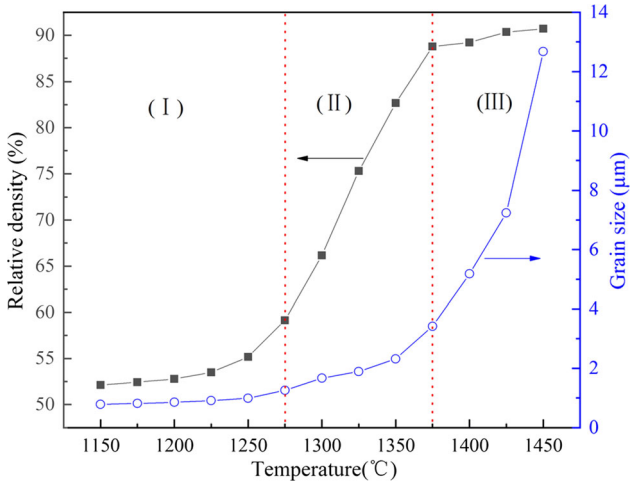

Fig. 3 Sintering kinetics window of $NiFe_2O_4$ ceramic by pressureless sintering

the relative density increased distinctly. The cooperation of particle rearrangement and increased interfacial atomic diffusion from higher temperature were the mainly effective factors to dominate densification process. (III): the final stage (relative density $>$ 88.78%, $>$ 1375°C): the grain growth became absolutely dominant while the densification was entirely dominated by interfacial atomic diffusion. There were only closed pores remained in the sintered ceramics while open pores were completely eliminated. The above-mentioned sintering kinetics window analysis was in keeping with the microstructure evolution, mainly shown in the insets of Fig. 2(a).

The introduction of nanopowder not only can improve the slurry stability, but also can influence the consolidation process. The initial sintering stage is particularly important in high density nanocomposites manufacturing for the densification in the initial stage can be accelerated for the high specific surface area (Ref 27). Hence, it is extremely significant to investigate the densification mechanism for the initial sintering stage.

Based on the researches of Bannister (Ref 28), Keski and Cutler (Ref 29) and Woolfrey and Bannister (Ref 30), the linear shrinkage of initial stage was utilized to calculate the sintering activation energy of initial stage. The specific calculation processes were presented in our previous research (Ref 22, 31). Firstly, three heating rates, C, namely 5, 10 and 20°C/min, were adopted to plot the curve of $\ln(\triangle L/L_0)_T$ against $\ln C$. The linear fitting slope of $\ln(\triangle L/L_0)_T$ against $\ln C$, was equal to $-1/(m+1)$, and the exponent m can be obtained. Secondly, linear fitting slope of $\ln[(\triangle L/L_0)/T]$ versus $1/T$ was used to obtain sintering activation energy of initial stage (Q), where the slope was equal to $-\frac{Q}{(m+1)R}$. The exponent m and sintering activation energy of initial stage were 1.406 and 268.34 kJ mol^{-1}, respectively, which were both mildly lower than these for high density $NiFe_2O_4$ ceramics consisted of 10 wt.% $NiFe_2O_4$ nanoparticles and 5 wt.% nano-binder, whose values were 1.506 and 295.11 kJ mol^{-1} (Ref 31). Under the same synthesis conditions, more $NiFe_2O_4$ nanoparticles were conducive to improve the sintering activity; as a result, the sintering activation energy was slightly decreased. According to the suggestion by Bannister (Ref 28), the densification controlling mechanism can be dominated according to the exponent m, where $m = 0$, 1 and 2 for viscous flow, volume diffusion and grain boundary diffusion, respectively. It can be derived that the initial stage of sintering process was controlled by both volume diffusion and grain boundary diffusion mechanisms for $m = 1.406$. More $NiFe_2O_4$ nanoparticles in the $NiFe_2O_4$ green body would be beneficial to heighten the atomic diffusion capacity and shorten the atomic diffusion path, therefore, the mass transport would be preferred by volume diffusion.

3.2 Grain Growth Kinetics

In order to make out the grain coarsening mechanisms, it was necessary to make great efforts on the grain growth kinetic analysis. Grain growth depends on sintering temperature and time, and the phenomenological grain growth kinetics can be articulated as (Ref 32).

$$G^n - G_0^n = K_0 \cdot t \cdot \exp\left(-\frac{Q}{RT}\right) \quad \text{(Eq 2)}$$

where G is the average grain size at sintering time t, G_0 is the initial grain size, n is denoted as the value of kinetic grain growth exponent, Q is defined as apparent activation energy for grain growth, K_0 is a pre-exponential constant, R is the ideal gas constant, and T is the absolute temperature, respectively. In this study, the initial grain size G_0 was about 328 nm according to the SEM of green body (not shown). The average grain size G of sintered sample was more than 3.393 μm, which was at least one order of magnitude more than G_0. So the G_0 was considerably smaller than G, G_0^n can be neglected relative to G^n (i.e., $G^n \gg G_0^n$, $n > 1$). Consequently, Eq 2 can be simplified as:

$$G^n = K_0 \cdot t \cdot \exp\left(-\frac{Q}{RT}\right) \quad \text{(Eq 3)}$$

Taking natural logarithm on both sides, Eq 3 can be modified as:

$$\ln G = \frac{1}{n}\ln t + \frac{1}{n}K_0 - \frac{Q}{nR}\frac{1}{T} \quad \text{(Eq 4)}$$

The n value in Eq 4 can be calculated by the slope of $\ln G \sim \ln t$ curve. As the value of n is known, the Q value can be calculated by the slope of the $\ln G \sim T^{-1}$ curve. Faster grain growth rates can be deduced according to smaller n and Q values (Ref 33).

Firstly, the grain growth exponent (n) at different temperatures would be calculated from the reciprocal of the slope of $\ln G$ versus $\ln t$ plot. Figure 4 illustrates the linear fitted curves of $\ln G \sim \ln t$ for $NiFe_2O_4$ ceramics sintered at different temperatures. The calculated n values are listed in Table 2. The related correlation coefficients (R^2, shown in Fig. 4) were quite high (0.979-0.988), indicating the data were stable and reliable. As shown in Table 2, it indicated that the value of n reduced with the increasing sintering temperature, in accordance with the acceleration of grain growth at high temperature. With the increase of temperature, the grain growth rates were accelerated obviously, that is to say, the curves were displaced upward to the larger grain sizes. It was found that the sintering of $NiFe_2O_4$ ceramic did not exhibit a parabolic grain growth for the n was larger than 2, i.e., between 2 and 3. However, the n approached gradually to 2 as the sintering temperature increased, implying a normal grain growth at high temperature (Ref 34). The reason to explain this phenomenon was that the diffusion rate was forcefully enhanced by the increasing temperature. Despite the addition of $NiFe_2O_4$ nanoparticles and nano-binder, no liquid phase would form during sintering at these temperatures. In the solid-phase sintering process, material migration depends mainly on the atomic diffusion between solid-phase particles. The atomic self-diffusion (consisting of volume diffusion, grain boundary diffusion and surface diffusion) coefficient D can be expressed as (Ref 35).

$$D = D_0 \exp\left(-\frac{\Delta Q}{RT}\right) \quad \text{(Eq 5)}$$

where D_0 is a constant, and ΔQ is the self-diffusion activation energy. According to formula (5), the atomic self-diffusion coefficient D increases exponentially with sintering temperature. Thus, the grain grew notably. As a result, the higher the sintering temperature, the lower the grain growth exponent (n) was.

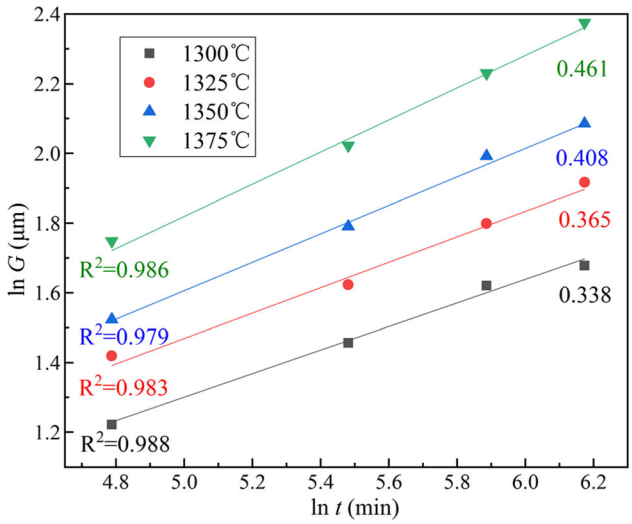

Fig. 4 The linear fitted curves of $\ln G \sim \ln t$ of $NiFe_2O_4$ ceramics sintered at different temperatures

Table 2 Calculated grain growth exponent values (n) at different temperatures

Temperature, °C	1300	1325	1350	1375
n	2.959	2.740	2.451	2.169

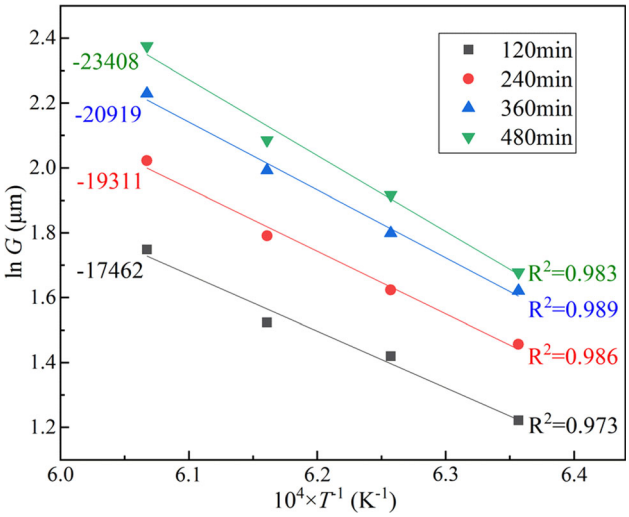

Fig. 5 Relationship curves between lg$G$ and T^{-1} of $NiFe_2O_4$ ceramics for different holding time

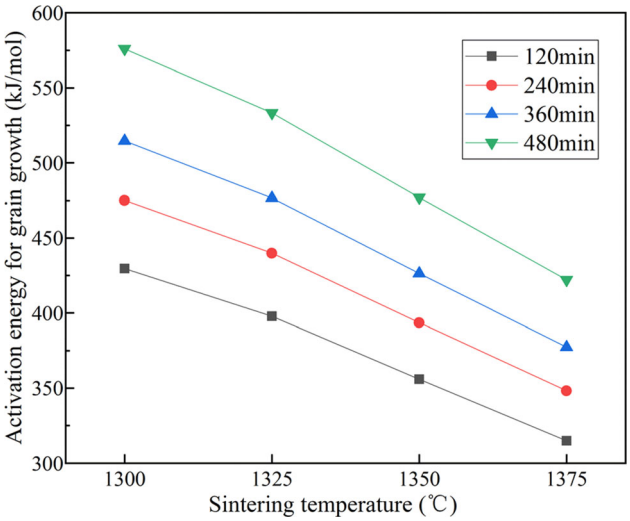

Fig. 6 Effects of sintering temperature and holding time on activation energies for grain growth

Secondly, the activation energy for grain growth in $NiFe_2O_4$ ceramic was calculated according to the relation between ln$G$ and inverse temperature ($10^4/T$). Figure 5 shows the effects of sintering temperature on grain size on a logarithm plot for different holding times. The slope of the line, calculated by the regression analysis technique, was used to calculate the activation energy on the basis of Eq 4. The estimated values and variation tendencies of activation energy for grain growth were displayed in Fig. 6. As you can see from the figure, the activation energy for grain growth increased with the decrease of sintering temperature when the holding time was constant,

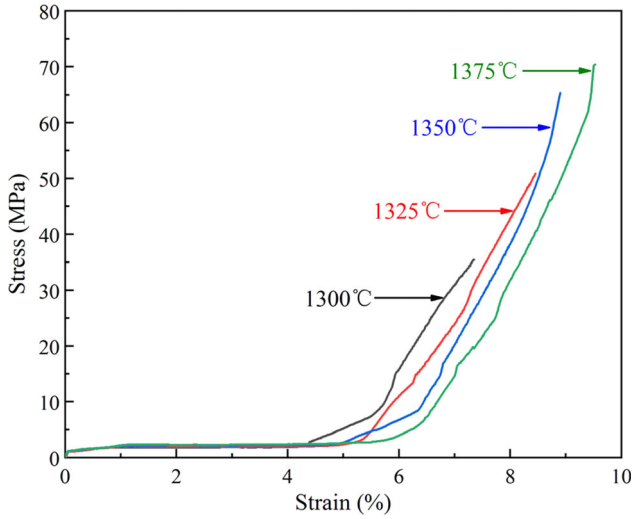

Fig. 7 Stress-strain curves of $NiFe_2O_4$ ceramics sintered at different temperatures

and increased with the extended holding time at the same sintering temperature. These variation tendencies were in accord with the confirmation by Wang et al. (Ref 36). The effect of sintering temperature on exponent n and corresponding activation energy for grain growth was consistent with that of grain size. In this work, the activation energy for grain growth only depended on the sintering temperature and holding time for the same green composition. With increasing temperature of sintering, more activated molecules were generated, therefore greater driving force for grain growth was available. As a result, the activation energy for grain growth decreased since the grains grew obviously. When the holding time was relatively short, most grains kept the original state with relatively smaller grain size. Hence, there were more residual defects, originated from the ball-milling process for preparing slurry, existent in lattice. The diffusion rate of atoms in defective crystals was higher than that in intact crystal, so the activation energy for grain growth was comparatively small. The lattice evolution tended to come complete, and the gains grew up obviously as the holding time increased continuously. As a consequence, the surface activity would be exhausted distinctly for the reduced defects. Moreover, the $NiFe_2O_4$ would be partly decomposed to NiO and Fe_2O_3 during the high temperature sintering process, and the nano-binder would react with Fe_2O_3 to generate new spinel phases, i.e., $MgFeAlO_4$, $MgFe_2O_4$ and Fe_2SiO_4 (Ref 22). When the holding time was short, the formation of new spinel phases would promote atomic diffusion. With the increase of holding time, the existence of newly formed spinel acted as barrier to hinder the grain boundary movement. The grain growth resistance increased prominently, so the activation energy for grain growth would be increased (Ref 37). In this research, the higher the sintering temperature, the lower the activation energy for grain growth was. In consequence, it was implied that the grain growth process was dominated by atomic diffusion.

3.3 Mechanical Properties

The stress–strain curves of $NiFe_2O_4$ ceramics sintered at various temperatures for 6 h were illustrated in Fig. 7. The stress–strain curves were obtained by means of three-point

bending test. It was obvious that all the stress–strain curves were alike, exhibiting typical brittle material characteristics. The ceramics will be fractured instantaneously without obvious plastic deformation when the critical load reached. The bending strength and elastic modulus values of $NiFe_2O_4$ ceramics sintered at different temperatures were indicated in Table 3. As shown in Table 3, both the bending strength and elastic modulus presented a clear ascending trend with increasing sintering temperature, despite the variation of elastic modulus was comparatively small. The SEM images of fracture surfaces of samples sintered at various temperatures for 6 h were exhibited in Fig. 8. The grain sizes and relative densities of the specimens sintered at different temperatures were illustrated in Table 3. As shown in Fig. 8(a), the grains grew on a relatively small scale at 1300°C. The intergranular interspaces were larger, and the grain boundary bonding strengths were lower. With increased sintering temperature, the micropores were sustainedly eliminated as a result of gradual grain growth and close combination of grains. When the sintering temperature was 1350°C, the relative density increased to 98.94%, and the grains sequentially grew, resulting in large grains and low porosity. As the temperature increased to 1375°C, the grains grew further and packed more closely, even though the relative density decreased slightly owing to the formation of intracrystalline pores for the enhanced sintering densification rate. As shown in Fig. 8, as the sintering temperature increased, the grains combined more closely, and pores became less and smaller, i.e., the porosity and pore size (defect size) decreased, which leaded to an increase in the stress value that the material can withstand without cracking. Additionally, transcrystalline fracture for larger grains consumed more energy in this condition. As a consequence, the bending strength of the sintered $NiFe_2O_4$ ceramics was clearly enhanced. The elastic modulus is sensitive to the porosity of the sintered $NiFe_2O_4$ ceramics and is inversely proportional to porosity (Ref 38). The larger the porosity is, the smaller the elastic modulus is. The increase of elastic modulus was mainly attributed to the relatively dense microstructure. More effects should be taken to analyze and verify the strengthening mechanism of the sintered $NiFe_2O_4$ ceramics.

Table 3 Mechanical properties of $NiFe_2O_4$ ceramics sintered at different temperatures

Temperature, °C	Grain size, μm	Relative density, %	Bending strength, MPa	Elastic modulus, GPa
1300	5.06 ± 0.36	95.23 ± 0.32	35.42 ± 1.12	2.95 ± 0.42
1325	6.05 ± 0.49	97.08 ± 0.21	50.83 ± 1.15	3.11 ± 0.46
1350	7.33 ± 0.65	98.99 ± 0.11	65.28 ± 0.90	3.26 ± 0.45
1375	9.30 ± 0.84	98.21 ± 0.18	70.36 ± 1.03	3.44 ± 0.53

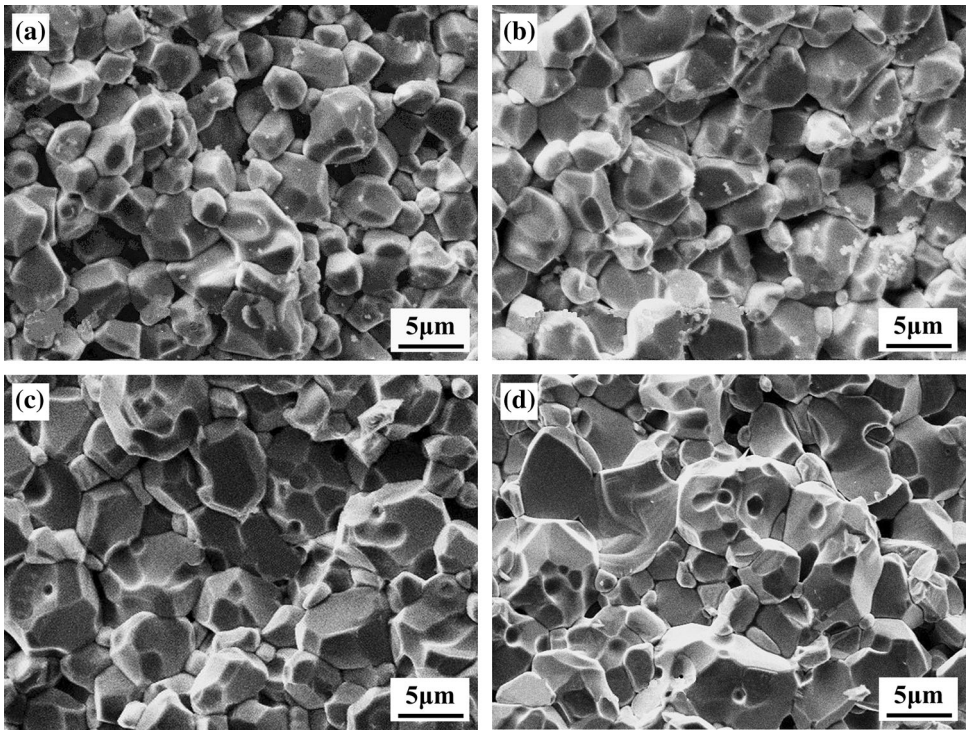

Fig. 8 SEM images of fracture surfaces of $NiFe_2O_4$ ceramics sintered at different temperatures for 6 h: (a) 1300°C, (b) 1325°C, (c) 1350°C, (d) 1375°C

4. Conclusion

Slip casting and pressureless sintering was adopted to fabricate $NiFe_2O_4$ ceramic. The green bodies showed obvious sintering shrinkage above 1100°C. With increasing sintering temperature, the linear shrinkage and linear shrinkage rate of the green body in the axial and radial directions increased simultaneously. The maximum densification rate was obtained at about 1316.5°C while the relative density was around 72%. The pressureless sintering kinetics window exhibited that the sintering process was divided into three stages, i.e., the initial stage, the intermediate stage and the final stage. The activation energy of initial sintering stage was 268.34 $kJ{\cdot}mol^{-1}$, and the initial stage of sintering process was dominated by both grain boundary diffusion and volume diffusion mechanisms. The kinetic analysis of grain growth illustrated the grain growth exponent (n) reduced with increased sintering temperature, while the activation energy for grain growth decreased with the elevated sintering temperature and the shortening of the holding time. The minimum values of n and activation energy for grain growth were 2.169 and 314.89 $kJ{\cdot}mol^{-1}$, respectively, when the sample was sintered at 1375°C for 120 min. It implied that the atomic diffusion process controlled the grain growth. The bending strength and elastic modulus increased from 35.42 ± 1.12 MPa and 2.95 ± 0.42 GPa to 70.36 ± 1.03 MPa and 3.44 ± 0.53 GPa, respectively, with the increase of sintering temperature from 1300 to 1375°C. The increases of bending strength and elastic modulus were mainly associated with the relatively dense microstructure.

Acknowledgments

Financial supports from the Fundamental Research Funds for the Central Universities (No. N182504015), Liaoning Revitalization Talents Program (No. XLYC1902097) and Program Liaoning Innovation Talents in University (No. LR2018011), were gratefully acknowledged.

References

1. B. Wang, J.J. Du, Y.H. Liu, and G.C. Yao, Effect of TiO_2 Doping on the Sintering Process, Mechanical and Magnetic Properties of $NiFe_2O_4$ Ferrite Ceramics, *Int. J. Appl. Ceram. Technol.*, 2015, **12**(3), p 658–664
2. K.E. Sickafus, J.M. Wills, and N.W. Grimes, Structure of Spinel, *J. Am. Ceram. Soc.*, 1999, **82**(12), p 3279–3292
3. A.T. Nelson, J.T. White, D.A. Andersson, J.A. Aguiar, K.J. McClellan, D.D. Byler, M.P. Short, and C.R. Stanek, Thermal Expansion, Heat Capacity, and Thermal Conductivity of Nickel Ferrite ($NiFe_2O_4$), *J. Am. Ceram. Soc.*, 2014, **97**(5), p 1559–1565
4. S. Briceño, W. Brämer-Escamilla, P. Silva, J. García, H. Del Castillo, M. Villarroel, J.P. Rodriguez, M.A. Ramos, R. Morales, and Y. Diaz, $NiFe_2O_4$/Activated Carbon Nanocomposite as Magnetic Material from Petcoke, *J. Magn. Magn. Mater.*, 2014, **360**, p 67–72
5. V. Manikandan, J.C. Denardin, S. Vigniselvan, and R.S. Mane, Structural, Dielectric and Enhanced Soft Magnetic Properties of Lithium (Li) Substituted Nickel Ferrite ($NiFe_2O_4$) Nanoparticles, *J. Magn. Magn. Mater.*, 2018, **465**, p 634–639
6. K. Kombaiah, J.J. Vijaya, L.J. Kennedy, and K. Kaviyarasu, Catalytic Studies of $NiFe_2O_4$ Nanoparticles Prepared by Conventional and Microwave Combustion Method, *Mater. Chem. Phys.*, 2019, **221**, p 11–28
7. Y. Tang, C.H. Yang, Y.W. Yang, X.T. Yin, W.X. Que, and J.F. Zhu, Three Dimensional Hierarchical Network Structure of S-$NiFe_2O_4$ Modified Few-Layer Titanium Carbides (MXene) Flakes on Nickel Foam as a High Efficient Electrocatalyst for Oxygen Evolution, *Electrochim. Acta*, 2019, **296**, p 762–770
8. S.F. Zhang, W.H. Jiang, Y.W. Li, X.L. Yang, P. Sun, F.M. Liu, X. Yan, Y. Gao, X.S. Liang, J. Ma, and G.Y. Lu, Highly-Sensitivity Acetone Sensors based on Spinel-Type Oxide ($NiFe_2O_4$) through Optimization of Porous Structure, *Sens. Actuators B*, 2019, **291**, p 266–274
9. X.F. Wang, K.M. Sun, S.J. Li, X.Z. Song, L. Cheng, and W. Ma, Porous Javelin-Like $NiFe_2O_4$ Nanorods as n-Propanol Sensor with Ultrahigh-Performance, *ChemistrySelect*, 2018, **3**(45), p 12871–12877
10. D. Mandal, A. Gorai, and K. Mandal, Electromagnetic Wave Ttrapping in $NiFe_2O_4$ Nano-Hollow Spheres: An Efficient Microwave Absorber, *J. Magn. Magn. Mater.*, 2019, **485**, p 43–48
11. X.C. Gao, J.Q. Bi, W.L. Wang, H.Z. Liu, Y.F. Chen, X.X. Hao, X.N. Sun, and R. Liu, Morphology-Controllable Synthesis of $NiFe_2O_4$ Growing on Graphene Nanosheets as Advanced Electrode Material for High Performance Supercapacitors, *J. Alloys Compd.*, 2020, **826**, p 154088 (1–10)
12. S.B. Bandgar, M.M. Vadiyar, Y.C. Ling, J.Y. Chang, S.H. Han, A.V. Ghule, and S.S. Kolekar, Metal Precursor Dependent Synthesis of $NiFe_2O_4$ Thin Films for High Performance Flexible Symmetric Supercapacitor, *ACS Appl. Energy Mater.*, 2018, **1**(2), p 638–648
13. J.J. Du, Y.H. Liu, G.C. Yao, Z.S. Hua, X.L. Long, and B. Wang, Microstructure, Mechanical Properties, and Pyroconductivity of $NiFe_2O_4$ Composite Reinforced with ZrO_2 Fibers, *J. Mater. Eng. Perform.*, 2013, **22**(6), p 1776–1782
14. P. Zarrabian, M. Kalantar, and S.S. Ghasemi, Fabrication and Characterization of Nickel Ferrite Based Inert Anodes for Aluminum Electrolysis, *J. Mater. Eng. Perform.*, 2014, **23**(5), p 1656–1664
15. D.W. Ni, K.B. Andersen, and V. Esposito, Sintering and Grain Growth Kinetics in $La_{0.85}Sr_{0.15}MnO_3$-$Ce_{0.9}Gd_{0.1}O_{1.95}$ (LSM-CGO) Porous Composite, *J. Eur. Ceram. Soc.*, 2014, **34**(15), p 3769–3778
16. H.D. Wu, W. Liu, L.F. Lin, Y.H. Li, Z. Tian, G.L. Nie, D. An, H.Z. Li, C.Y. Wang, Z.P. Xie, and S.H. Wu, Sintering Kinetics Involving Densification and Grain Growth of 3D printed Ce–ZrO_2/Al_2O_3, *Mater. Chem. Phys.*, 2020, **239**, p 122069 (1–6)
17. A. Talimian and D. Galusek, Aqueous Slip Casting of Translucent Magnesium Aluminate Spinel: Effects of Dispersant Concentration and Solid Loading, *Ceram. Int.*, 2019, **45**(8), p 10646–10653
18. Y.H. Sun, W.H. Xiong, C.H. Li, and L. Yuan, Effect of Dispersant Concentration on Preparation of an Ultrahigh Density ZnO-Al_2O_3 Target by Slip Casting, *J. Am. Ceram. Soc.*, 2009, **92**(9), p 2168–2171
19. K. Moritz, N. Gerlach, J. Hubálková, and C.G. Aneziris, Pressure Slip Ccasting of Coarse-Grained Alumina-Carbon Materials, *Int. J. Appl. Ceram. Technol.*, 2019, **16**(1), p 14–22
20. Y. Liu, Y.C. Shu, X.Y. Zeng, B.S. Sun, P. Liang, Y. Zhang, C. Qiu, J.H. Yi, and J.L. He, Study on the Sintering Behavior and Characterization of the IGZO Ceramics by Slip Casting, *Int. J. Appl. Ceram. Technol.*, 2019, **16**(2), p 585–594
21. X.N. Sun, H.K. Wu, G.Z. Zhu, Y.C. Shan, J.J. Xu, J.T. Li, and E.A. Olevsky, Direct Coarse Powder Aqueous Slip Casting and Pressureless Sintering of Highly Transparent AlON Ceramics, *Ceram. Int.*, 2020, **46**(4), p 4850–4856
22. Z.G. Zhang, J.R. Xu, Z.K. Cao, and G.C. Yao, Fabrication of High-Density $NiFe_2O_4$ Ceramics by Slip Casting and Pressureless Sintering, *Int. J. Appl. Ceram. Technol.*, 2020, **17**(4), p 1811–1821
23. Z.G. Zhang, G.C. Yao, X. Zhang, J.F. Ma, and H. Lin, Synthesis and Characterization of Nickel Ferrite Nanoparticles via Planetary Ball Milling Assisted Solid-State Reaction, *Ceram. Int.*, 2015, **41**(3 Part B), p 4523–4530
24. S. Mitra, A.R. Kulkarni, and O. Prakash, Densification Behavior and Two Stage Master Sintering Curve in Lithium Sodium Niobate Ceramics, *Ceram. Int.*, 2013, **39**(S1), p S65–S68
25. W. Liu, Z.P. Xie, and L. Cheng, Sintering Kinetics Window: An Approach to the Densification Process during the Preparation of Transparent Alumina, *Adv. Appl. Ceram.*, 2015, **114**(1), p 33–38
26. D. An, W. Liu, Z.P. Xie, H.Z. Li, X.D. Luo, H.D. Wu, M.P. Huang, J.W. Liang, Z. Tian, and R.X. He, A Strategy for Defects Healing in 3D Printed Ceramic Compact via Cold Isostatic Pressing: Sintering Kinetic Window and Microstructure Evolution, *J. Am. Ceram. Soc.*, 2018, **102**(5), p 2263–2271
27. M. Lakusta, I. Danilenko, G. Volkova, L. Loladze, V. Burkhovetskiy, O. Doroshkevich, I. Brykhanova, I. Popova, and T. Konstantinova,

Sintering Kinetics of ZrO_2 Nanopowders Modified by Group IV Elements, *Int. J. Appl. Ceram. Technol.*, 2019, **16**(4), p 1481–1492
28. M.J. Bannister, Shape Sensitivity of Initial Sintering Equations, *J. Am. Ceram. Soc.*, 1968, **51**(10), p 548–553
29. J.R. Keski and I.B. Cutler, Initial Sintering of MnXO-Al_2O_3, *J. Am. Ceram. Soc.*, 1968, **51**(8), p 440–444
30. J.L. Woolfrey and M.J. Bannister, Nonisothermal Techniques for Studying Initial-Stage Sintering, *J. Am. Ceram. Soc.*, 1972, **55**(8), p 390–394
31. Z.G. Zhang, X.T. Lu, and J.L. Liu, $NiFe_2O_4$ Ceramic U-shaped Sleeve Prepared by Slip Casting and Pressureless Sintering, *J. Inorg. Mater.*, 2020, **35**(6), p 661–668
32. T. Senda and R.C. Bradt, Grain Growth in Sintered ZnO and ZnO-Bi_2O_3 Ceramics, *J. Am. Ceram. Soc.*, 1990, **73**(1), p 106–114
33. W.Y. Du, Y.L. Ai, W.H. Chen, W. He, J.J. Zhang, Y.Q. Fan, and Y.X. Gong, Grain Growth Kinetics and Growth Mechanism of Columnar Al_2O_3 Crystals in $x$$Nb_2O_5-7.5La_2O_3$-$Al_2O_3$ Ceramic Composites, *Ceram. Int.*, 2019, **45**(6), p 6788–6794
34. M. Vaidya, A. Anupam, J.V. Bharadwaj, C. Srivastava, and B.S. Murty, Grain Growth Kinetics in CoCrFeNi and CoCrFeMnNi High Entropy A Processed by Spark Plasma Sintering, *J Alloys Compd.*, 2019, **791**, p 1114–1121
35. S.J. Guo, *Powder Sintering Theory*, Metallurgical Industry Press, Beijing, 1998
36. B. Wang, J.J. Du, Z. Fang, and P. Hu, Effect of TiO_2 Addition on Grain Growth, Anodic Bubble Evolution and Anodic Overvoltage of $NiFe_2O_4$-Based Composite Inert Anodes, *J. Mater. Eng. Perform.*, 2017, **26**(11), p 5610–5619
37. Y. Liu, Y.L. Ai, W. He, W.H. Chen, and J.J. Zhang, Grain Growth Kinetics in Microwave Sintered Graphene Platelets Reinforced ZrO_2/Al_2O_3 Composites, *Ceram. Int.*, 2018, **44**(14), p 16421–16427
38. D.C. Jia and G.M. Song, *Properties of Inorganic Nonmetallic Materials*, Science Press, Beijing, 2008